Biofouling

The Journal of Bioadhesion and Biofilm Research

ISSN: 0892-7014 (Print) 1029-2454 (Online) Journal homepage: www.tandfonline.com/journals/gbif20

Characterization of organic fouling on thermal bubble-driven micro-pumps

Brandon Hayes, Cillian Murphy, Janeth Marquez Rubio, Daimean Solis, Kaushik Jayaram & Robert MacCurdy

To cite this article: Brandon Hayes, Cillian Murphy, Janeth Marquez Rubio, Daimean Solis, Kaushik Jayaram & Robert MacCurdy (2024) Characterization of organic fouling on thermal bubble-driven micro-pumps, Biofouling, 40:3-4, 290-304, DOI: 10.1080/08927014.2024.2353034

To link to this article: https://doi.org/10.1080/08927014.2024.2353034

BIOFOULING
2024, VOL. 40, NOS. 3–4, 290–304
https://doi.org/10.1080/08927014.2024.2353034

Taylor & Francis
Taylor & Francis Group

Characterization of organic fouling on thermal bubble-driven micro-pumps

Brandon Hayes[a], Cillian Murphy[a,b], Janeth Marquez Rubio[c], Daimean Solis[c], Kaushik Jayaram[a] and Robert MacCurdy[a]

[a]Paul M. Rady Department of Mechanical Engineering, University of Colorado Boulder, Boulder, Colorado, USA; [b]School of Mechanical and Materials Engineering, University College Dublin, Dublin, Ireland; [c]Department of Biomedical Engineering, University of Colorado Boulder, Boulder, Colorado, USA

ABSTRACT

Thermal bubble-driven micro-pumps are an upcoming micro-actuator technology that can be directly integrated into micro/mesofluidic channels, have no moving parts, and leverage existing mass production fabrication approaches. These micro-pumps consist of a high-power micro-resistor that boils fluid in microseconds to create a high-pressure vapor bubble which performs mechanical work. As such, these micro-pumps hold great promise for micro/mesofluidic systems such as lab-on-a-chip technologies. However, to date, no current work has studied the interaction of these micro-pumps with biofluids such as blood and protein-rich fluids. In this study, the effects of organic fouling due to egg albumin and bovine whole blood are characterized using stroboscopic high-speed imaging and a custom deep learning neural network based on transfer learning of RESNET-18. It was found that the growth of a fouling film inhibited vapor bubble formation. A new metric to quantify the extent of fouling was proposed using the decrease in vapor bubble area as a function of the number of micro-pump firing events. Fouling due to egg albumin and bovine whole blood was found to significantly degrade pump performance as well as the lifetime of thermal bubble-driven micro-pumps to less than 10^4 firings, which may necessitate the use of protective thin film coatings to prevent the buildup of a fouling layer.

ARTICLE HISTORY
Received 19 December 2023
Accepted 2 May 2024

KEYWORDS
biofouling; microfluidics; mesofluidics; phase change; inertial pumping

Introduction

Microfluidics has the potential to revolutionize healthcare by enabling point-of-care testing and diagnostics in regions lacking centralized healthcare infrastructure (Chin et al. 2011; Mohammed et al. 2015; Preetam et al. 2022). Termed lab-on-a-chip systems, such technology has the potential to integrate entire medical diagnostic laboratories on a handheld device. To date, lab-on-a-chip systems have been demonstrated and utilized for a wide variety of medical and biomedical applications such as cell culturing (Hung et al. 2005; Gómez-Sjöberg et al. 2007), polymerase chain reaction (PCR) analysis (Marcus et al. 2006; Zhang et al. 2006), drug delivery (Liu et al. 2017; 2022), blood filtration (Yang et al. 2006; Nivedita and Papautsky 2013), and cancer screening (Salim et al. 2017; Hashemzadeh et al. 2021). However, commercial lab-on-a-chip systems often require large, bulky pump sources to move fluid which increases the size of the entire system; that is, while the actual microfluidic device may be micro-scale or meso-scale, the pump source often is the dominant size scale for a lab-on-a-chip system leading to the current adage of "lab-on-a-chip or chip-in-a-lab" (Mohammed et al. 2015). Thermal bubble-driven micro-pumps (also known as inertial micro-pumps) are an upcoming micro-actuation technology for moving fluid without the use of external pump sources or moving parts and can be directly integrated into micro/mesofluidic channels using existing mass fabrication infrastructure (Torniainen et al. 2012; Hayes et al. 2018; Kornilovitch et al. 2022). Thus, these micro-pumps hold great potential for enabling truly lab-on-a-chip technologies. Yet, to date, little work has studied the interaction of these micro-pumps with biofluids. In a realistic microfluidic biomedical application, the micro-pump will be in contact with protein-rich and cell-laden fluids which can induce fouling of these micro-pumps and degrade performance and lifetime. As such, understanding organic fouling on thermal

---

CONTACT Robert MacCurdy ✉ maccurdy@colorado.edu

Supplemental data for this article can be accessed online at https://doi.org/10.1080/08927014.2024.2353034.

bubble-driven micro-pumps is critical to utilization of this technology in healthcare.

Thermal bubble-driven micro-pumps were first theorized and demonstrated by Prosperetti et al. (Yuan and Prosperetti 1999; Ory et al. 2000; Yin and Prosperetti 2005) in the 2000s and later developed for pumping aqueous fluids by Hewlett–Packard Inc (Torniainen et al. 2012). around 2010. Based on thermal inkjet (TIJ) technology, these micro-pumps consist of a micro-resistor that locally boils liquid in a micro-channel generating a vapor bubble which performs mechanical work. A voltage pulse lasting a few microseconds superheats an interfacial layer of fluid above the resistor's surface close to its critical point (approximately $300\,^{\circ}C$ for water) which causes explosive boiling (Einat and Grajower 2010). The high-pressure vapor bubble rapidly expands in the channel until its internal pressure falls below atmospheric pressure upon which the bubble collapses (Govyadinov et al. 2016). Since the vapor bubble forms in a subcooled liquid, after bubble collapse, the vapor bubble re-dissolves back into the fluid (Einat and Grajower 2010). When placed asymmetrically in a micro-channel with reservoirs at either end, the momentum imbalance upon bubble collapse creates a net fluid pumping effect for each actuation (Kornilovitch et al. 2013; 2022).

Fouling can be broadly divided into four main categories: scaling and mineral fouling, particle fouling, biofouling, and organic fouling (Bhattacharjee et al. 2016). Scaling and mineral fouling occurs when inorganic material precipitates onto a surface as is common in reverse osmosis membranes (Supekar et al. 2018). Particle fouling occurs when solid particles suspended in a fluid accumulate on a surface (Henry et al. 2012). Biofouling occurs when microorganisms adhere to a surface and can cause the formation of a biofilm (Schultz 2007). And, lastly, organic fouling, which is the focus of this work, occurs when organic substances such as proteins adhere to a surface (de Almeida et al. 2023). To our knowledge, no published work to date has investigated organic fouling on thermal bubble-driven micro-pumps. Nevertheless, thermal bubble-driven micropumps reach high temperatures and can be considered to be similar to high temperature plate heat exchangers; thus, we leverage literature from heat exchangers and fouling on heated surfaces in the food industry in which manipulation of proteins and organic material is commonplace, to understand the mechanism of fouling on thermal bubble-driven micropumps. Specifically, work by Jeurnink et al. and Elofsson et al. suggest that the primary step in fouling on milk processing equipment is the adsorption of a monolayer of proteins onto the wall of the heating surface (Elofsson et al. 1996; Jeurnink et al. 1996). The deposition rate is a function of the reaction rate for activated/unfolded proteins, their transport to the surface, and the subsequent adhesion probability (Jeurnink et al. 1996; Alhuthali et al. 2022). As the formation of the layer of organic material grows, the heat transfer coefficient is reduced (Mahdi et al. 2009). Specific to thermal bubble-driven micro-pumps, a reduction in the heat transfer coefficient results in increased resistor surface temperatures along with lower fluid interface temperatures. As such, a layer of organic material on a thermal bubble-driven micro-pump is expected to both induce failure (resistor burnout) as well as greatly influence vapor bubble dynamics and thus pump performance due to a reduction in the fluid interface temperature necessary to achieve stable bubble nucleation.

The present work studies the effect of organic fouling on vapor bubble dynamics of thermal bubble-driven micro-pumps in which fouling induces a layer of adsorbed organic material on the resistor's surface. In this work, we investigate organic fouling from egg albumin (ovalbumin) and defibrinated bovine whole blood dilutions using deep learning semantic image segmentation. To our knowledge, this is the first work to investigate organic fouling on thermal bubble-driven micro-pumps and to demonstrate the ability to form a thermal generated vapor bubble in blood. We demonstrate that organic fouling from egg albumin and defibrinated whole blood on fluorine-doped tin oxide (FTO) thin film resistors causes the vapor bubble volume to collapse, to near zero within 10^4 firing events for egg albumin, which greatly decreases resistor lifetime and performance. We envision that a realistic micro/mesofluidic system using thermal bubble-driven micro-pumps for healthcare will utilize protein-rich and cell-laden fluids. As such, this work provides a foundation to understand and characterize organic fouling of thermal bubble-driven micro-pumps.

Materials and methods

Electrical setup and driving electronics

Actuation of thermal bubble-driven micro-pumps requires a short, high-power pulse on the order of µs's which causes explosive boiling at the resistor's surface. In this study, we use a custom electrical setup to deliver fast (0.1-100 µs), high-power (0-1700 W) pulses capable of delivering 0-5.6 A at up to 0-300 V.

Specifically, the following pulse duration, τ, and pulse voltage, V, parameters were used for the 50×100, 180×420, 300×700, and 500×1000 μm^2 resistors: $\tau = 1.5$ μs and $V = 30$ V, $\tau = 5$ μs and $V = 90$ V, $\tau = 5$ μs and $V = 135$ V, $\tau = 5$ μs and $V = 165$ V respectively. All tests were performed with a firing frequency of 25 Hz unless otherwise stated. The driving electronics and complete bill of materials are detailed in our past work (Hayes et al. 2022). We stress that the voltages used in this system are *lethal* if handled improperly.

Stroboscopic imaging

Bubble expansion and collapse take approximately 100 μs for a 300×700 μm^2 resistor. As such, high-speed imaging is needed to characterize the vapor bubble dynamics. Here, we use a custom stroboscopic imaging system, see Figure 1, time synced to the aforementioned electrical system in which a high intensity LED light source (Lightspeed Technologies HPLS-36DD18B) and a Basler CMOS camera with a global shutter (a2A1920-160 umBAS) are used to enable high resolution stroboscopic high-speed imaging. The HPLS-36DD18B LED can be pulsed from 50 ns − 2 μs at a 1% duty cycle which sets the maximum effective frame rate of the system at 20 Mfps. A complete description of the imaging setup is discussed in our past work (Hayes et al. 2022). In this study, we image the vapor bubbles at $t = 10$ μs after the start of a firing pulse, for every firing event. As shown in Figure S1, the vapor bubble is consistently near its maximum expansion point at $t = 10$ μs which provides a stable metric for comparison of the vapor bubble area throughout the fouling process. An ideal resistor with no surface fouling would result in the same vapor bubble for each firing event; however, in the presence of surface fouling, the vapor bubble area will decrease which can be used as a metric for the extent and rate of organic fouling.

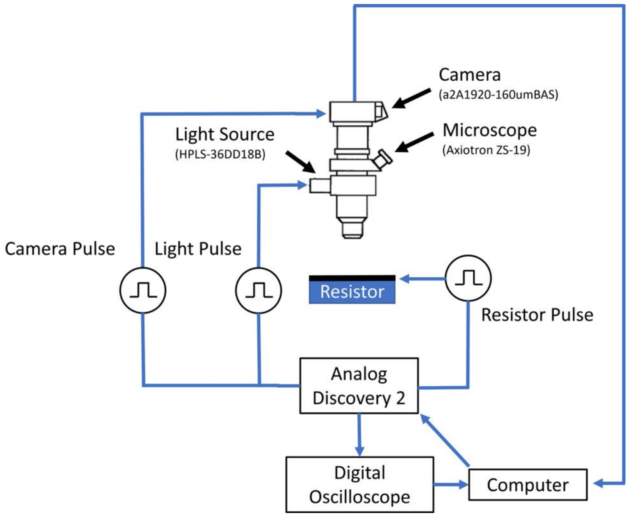

Figure 1. Stroboscopic imaging setup illustrates the custom stroboscopic imaging setup used to image vapor bubble dynamics. The system is capable of imaging at up to 20 Mfps.

Resistor fabrication

Laser cutting provides a way to rapidly fabricate single material, high-power resistors through a simple, quick non-fab process (by which we mean a non-semiconductor microfabrication workflow). Here, we use a Light Conversion CARBIDE-CB5 Femtosecond UV laser cutter which has an ALIO 6D Hybrid Hexapod stage and integrated SCANLAB excelliSCAN galvanometer positioning system with a spot size of approximately 5 μm enabling a minimum resolution of structures around 10 μm. The detailed workflow and femtosecond laser cutting parameters are described and characterized in our past work (Hayes et al. 2022).

Figure 2 summarizes the design and fabrication process for a thermal bubble-driven micro-pump. Fusion 360 was used to design resistor geometries. Resistors were designed to a target rectangular dimension (300×700 μm^2 in Figure 2a) and a 250 μm fillet was used to minimize hot spots near the edges of the resistor which can cause device failure (Bar-Levav et al. 2020). Once designed, resistors were fabricated by laser cutting commercial 8 Ω sq^{-1}, 340 nm fluorine-doped tin oxide (FTO) thin film coated glass (Sigma Aldridge, St. Louis, MO, USA). Femtosecond laser processing provides a non-fab method to rapidly fabricate thermal bubble-driven micro-pumps with near-fab resolution as shown by the Keyence VK-X1100 optical profilometer image in Figure 2b.

Biofluid preparation

For best imaging of organic fouling on thermal bubble-driven micro-pumps, the biofluid solution must be as transparent as possible. As such, egg albumin powder (HiMedia GRM6421100g) was dissolved in deionized (DI) water in two steps: (1) mechanical agitation and (2) ultrasonic mixing. In (1), albumin powder was added to deionized water and mixed using a hot plate with a stir rod at at $37\,^{\circ}C$ and rotational frequency 350 rpm for 15 min. In (2), the solution was immersed in an ultrasonic bath for 5 min (Vevor 15 L Ultrasonic Cleaner) to further break up albumin

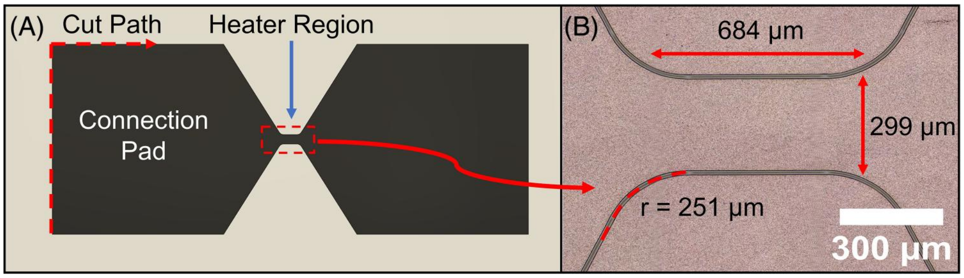

Figure 2. Resistor design and fabrication illustrates the design and fabrication of a 300 x 700 µm^2, 8 Ω sq^{-1} FTO resistor with 250 µm^2 fillets on each corner. (a) CAD software, Autodesk Fusion 360, was used to generate a .dxf file defining the resistor's cut path. Each resistor consists of two connection pads and a heater region. (b) key dimensions of the fabricated resistor were verified using a Keyence VK-X1100 optical profilometer. The FTO film was cut using the femtosecond UV laser cutter with the following cut settings: power = 0.643 W (100%), repetition frequency = 250 kHz, fluence = 7.00 J cm^{-2} , speed = 500 mm s^{-1} , and passes = 12.

particles and increase dissolution in water. Care must be taken to avoid premature denaturation of the protein solution during mixing.

In this study, defibrinated bovine whole blood (Innovative Research Inc.) was used to study the effect of biofouling on thermal bubble-driven micro-pumps from cell-laden fluids. Bovine blood was diluted with DI water to create different weight percent concentrations for testing.

Image processing

The use of protein-rich and cell-laden fluids such as egg albumin solution and bovine blood create non-ideal imaging situations. Namely, the solutions have dispersed particles obstructing view of the resistor, see Figure 3a. Additionally, fouling on the resistor's surface creates a residual film which is similar in appearance to the vapor bubble that makes identification and segmentation of the vapor bubble challenging. As such, conventional background subtraction image processing techniques successfully employed in our past work (Hayes et al. 2022) are not suitable for detection of fouling on the resistor's surface in this work. Therefore, we developed a deep learning semantic segmentation neural network workflow based on transfer learning of RESNET-18, which is using a pre-trained network and retraining it on additional new data, to identify and segment the vapor bubble area by training the pre-trained network on additional new data, in this study, images of the vapor bubble during fouling. We detail the steps in this workflow below, also displayed graphically in Figure 4.

1. *Load Training Data*. The base training data set consists of 121 labeled vapor bubble images at various stages of fouling and imaging conditions. This data set is the base case used to analyze each new test.
2. *Label 5 Images from Target Data Set*. Vapor bubble fouling data is recorded, approximately 10^4 images, and 5 sample images evenly distributed from the data set are manually labeled.
3. *Merge Data Sets*. The base case and 5 manually labeled images from the new data set are merged to form one combined data set of 126 labeled images.
4. *Train Network*. RESNET-18 is trained using MATLAB with MiniBatchSize = 5, MaxEpochs = 10, InitialLearningRate = 0.01, and ValidationFrequency = 5. The 126 labeled images are randomly divided into a training data set (60% of total images) and validation data set (40% of total images). We found that resistors of different sizes require separate networks to yield the most accurate results in segmenting the vapor bubble.

Bubble physics

Thermal bubble-driven micro-pumps are high-power, high-temperature, thin film resistors. A voltage pulse lasting a few microseconds superheats an interfacial layer of fluid above the resistor's surface close to its critical point (approximately *300 °C*) which causes explosive boiling. The resulting high-pressure vapor bubble rapidly expands and collapses which performs mechanical work. It is expected that organic fouling will occur over time on these micro-pumps due to the high working temperatures of the resistors during a microsecond heating pulse, measured at approximately *200 °C* in our past work for a 300 × 700 µm^2 resistor (Hayes et al. 2022). However, it is unknown to what extent fouling will impact vapor bubble dynamics. Since the vapor bubble dynamics drive fluid motion, it is important to understand the

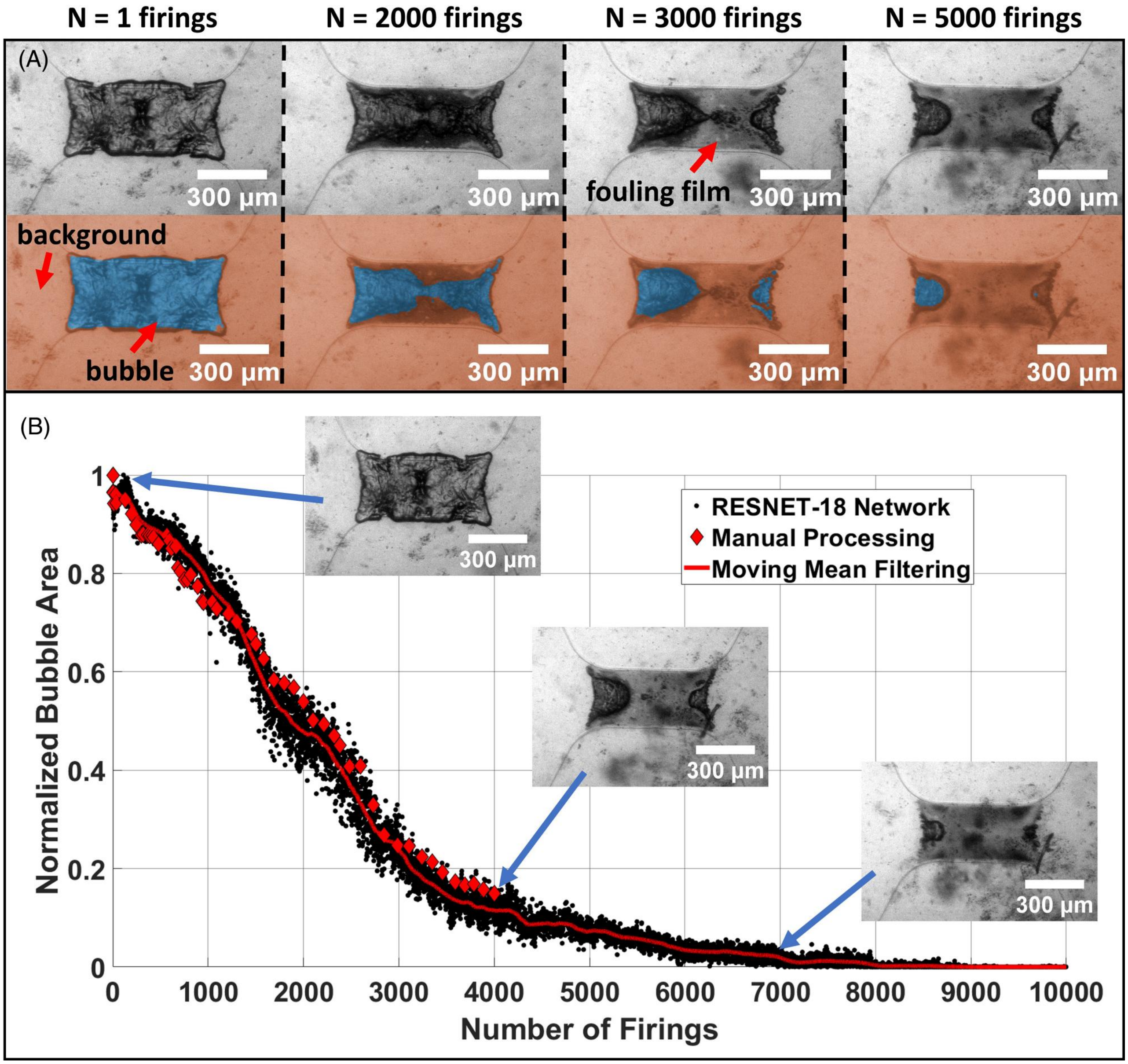

Figure 3. RESNET-18 transfer learning network validation depicts the result of transfer learning using RESNET-18 for organic fouling on a 300 x 700 μm^2 thermal bubble-driven micro-pump. Stroboscopic vapor bubble images were imaged with an 10 μs time delay from the onset of the firing pulse. The vapor bubble area decrease was used as a measure of organic fouling and residue buildup. The RESNET-18 network was trained in accordance to section "Image processing". A DI water solution of 1 g dL^{-1} albumin was utilized. In (a), the accuracy of the trained network is assessed in which snapshots of the vapor bubble at various number of firings is shown along with the predicted bubble area overlay. In (b), the bubble area is normalized to the max bubble area and a moving average filter, k = 200 data points, is applied. Manual bubble area tracking was performed to validate the results of the RESNET-18 network. The average error of the trained RESNET-18 network with manual processed data was 3.2%.

interaction between biofluids and fouling on thermal bubble-driven micro-pumps.

Vapor bubble dynamics of thermal bubble-driven micropumps consist of four stages: nucleation, expansion, collapse, and post-collapse. Figure 5 illustrates the vapor bubble dynamics for a 300×700 μm^2, 8 Ω sq^{-1}, 44.99 Ω FTO resistor with 250 μm fillets on each corner and water covering its surface. A firing pulse of $\tau = 5$ μs at $V = 100$ V was used to cause explosive boiling on the resistor's surface. The vapor bubble dynamics were imaged at 10 Mfps. Initially, the vapor bubble nucleates at the resistor's corners, $t = 3.5$ μs, where the heat flux is the greatest; after which, the vapor bubble grows and blankets the resistor's surface, $t = 5.0$ μs. The vapor bubble loses energy as it continues to expand reaching its maximum volume at $t = 12.0$ μs. Then, the vapor bubble rapidly collapses at high velocities which creates fluid jets impinging in the vapor upon collapse, $t = 39.2$ μs. During post-collapse, the vapor bubble collapse creates a region of low pressure which causes cavitation, $t = 41.5$ µs, and vapor bubble rebound until the vapor bubble fully dissolves back into the subcooled fluid, $t = 68.0$ µs.

We note that while the interfacial layer of fluid which boils exceeds the denaturation temperature of most protein and cell-laden fluids, *41 °C* (Lepock 1997), the bulk of the fluid remains under the denaturation temperature (CFD, XXXX). Additionally, there exists a "speed limit" for thermal protein damage during pulse heating. If the time duration of a heating pulse is below a certain threshold, proteins can be exposed to higher temperatures without denaturing (Steel et al. 2006). Thus, we expect that temperature sensitive fluids, such as protein and cell-laden fluids can be moved with thermal bubble-driven micro-pumps with an acceptable degree of degradation. However, a detailed analysis of the specific extent of protein and cell degradation due to transient heating from thermal bubble micro-pumps is beyond the scope of this work and will be the subject of future work. This manuscript focuses on the extent and impact of organic fouling on the surface of thermal bubble-driven micro-pumps as a function of the number of firing events for two specific biofluids and four different resistor sizes.

Organic fouling on thermal bubble-driven micro-pumps

Organic fouling of proteins on a surface is a complex process which can involve adsorption, desorption, and irreversible protein denaturation (Hedayati et al. 2020). Additionally, when proteins denature, hydrophobic amino acid residues become exposed making surface adsorption more favorable (Lu et al. 1998). In thermal bubble-driven micro-pumps, proteins can be denatured due to a combination of high temperatures and high strain rates (Lepock 1997; CFD, XXXX; Bogahawaththa and Vasiljevic 2022). Here, we assess the extent of surface fouling caused by egg albumin, and whole bovine blood dilutions in DI water.

Deep learning neural network validation for automatic image segmentation

We utilize the decrease in vapor bubble area as a measure of organic fouling which necessitates accurate segmentation of the vapor bubble. To do so, the RESNET-18 network, described in Figure 4, is validated against manually labeled vapor bubble areas for a 300×700 µm^2 resistor in a DI water solution of 1 g dL^{-1} egg albumin. For comparison, human whole blood has an albumin concentration of 3.4-5.4 g dL^{-1}. As shown in Figure 3a, the network successfully segments the vapor bubble even as the fouling film grows with increasing firing events. Furthermore, as depicted in Figure 3b, the average error between the trained network and manually labeled vapor bubble areas was 3.2% demonstrating the accuracy of the RESNET-18 semantic segmentation workflow. Vapor bubble area is normalized to the maximum area. A moving mean filter using $k = 200$ data points is applied to smooth the data. As shown in Figure 3b, a layer of organic residue rapidly forms and covers half of the active resistor area within $N = 2000$ firing events. By $N = 5000$ firings, the vapor bubble area has decreased to less than 10% of its initial area. Practically, a reduction in the vapor bubble area translates to a decrease in the per pulse flow rate of a thermal bubble-driven micro-pump. Thus, it is important to understand the fouling dynamics and impact on thermal bubble-driven micro-pumps in order to enable pumping of protein-rich and cell-laden fluids.

Fouling with egg albumin

To further characterize albumin protein fouling on thermal bubble-driven micro-pumps, four different size resistors (50×100, 180×420, 300×700, and 500×1000 µm^2) were fabricated and tested in a DI water solution of 1 g dL^{-1} egg albumin. With the fab-less microfabrication process used in this study, the lower dimensional resolution is approximately 50 µm. For each resistor size, the semantic segmentation workflow, detailed in Figure 4, was performed to generate a trained RESNET-18 network specific to a given resistor size. Figure 6 shows the decrease of the normalized vapor bubble area as a function of the number of firing events. Each resistor size consists of 5 sample replicates in which the solid line represents the mean of the moving averages for each sample replicate while the shaded area represents one standard deviation from the mean. It is evident that there is a large sample variability denoted by the standard deviation for each resistor size which is characteristic of fouling being a stochastic process. Across all resistor sizes, as the number of firing events increases, a protein residue grows on the resistor's surface which inhibits vapor bubble formation due to a reduction in the heat transfer rate. The protein residue growth is indicated by the reduction in the normalized vapor bubble area. The rate of protein residue growth was fastest at the onset for the 300×700 and 500×1000

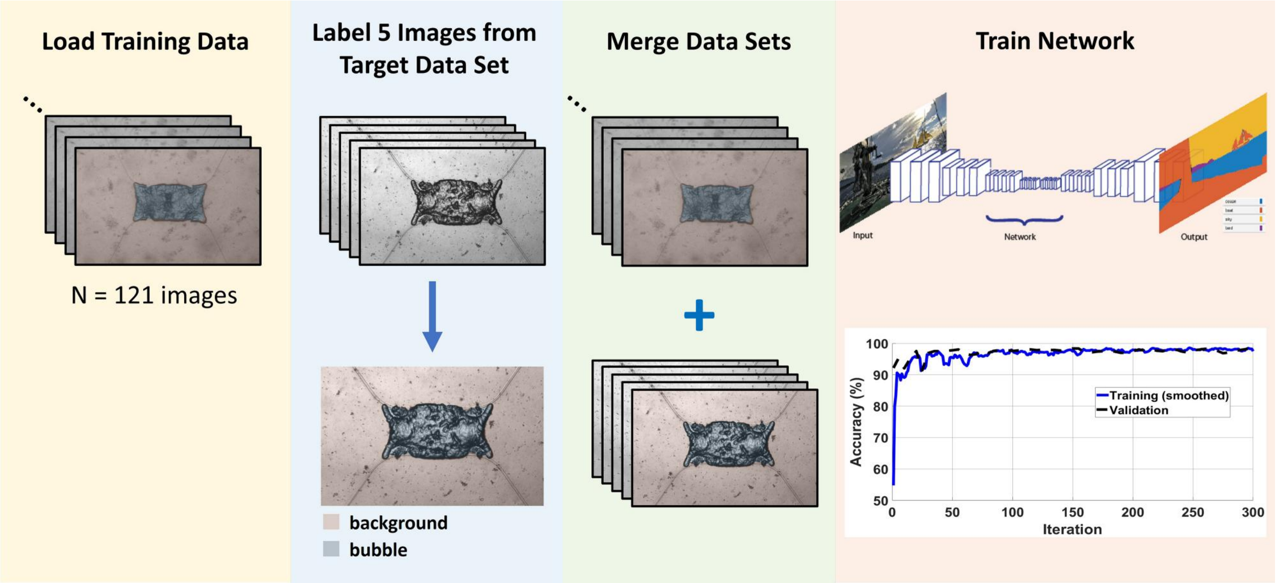

Figure 4. RESNET-18 transfer learning network training workflow left to right, describes the workflow to apply transfer learning of RESNET-18 for semantic segmentation of vapor bubbles. First, a training data set containing various size resistors, lighting conditions, and vapor bubble dynamics are labeled. Here, we labeled 121 images. Next, 5 images evenly distributed from the target data set to analyze are labeled with the first being the initial firing event and the remaining images spaced throughout the 10,000 images. Then, the training data set is merged with the manually labeled 5 images from the target data set. Last, the RESNET-18 network is trained using 60% of the images for training and 40% of the images for validation.

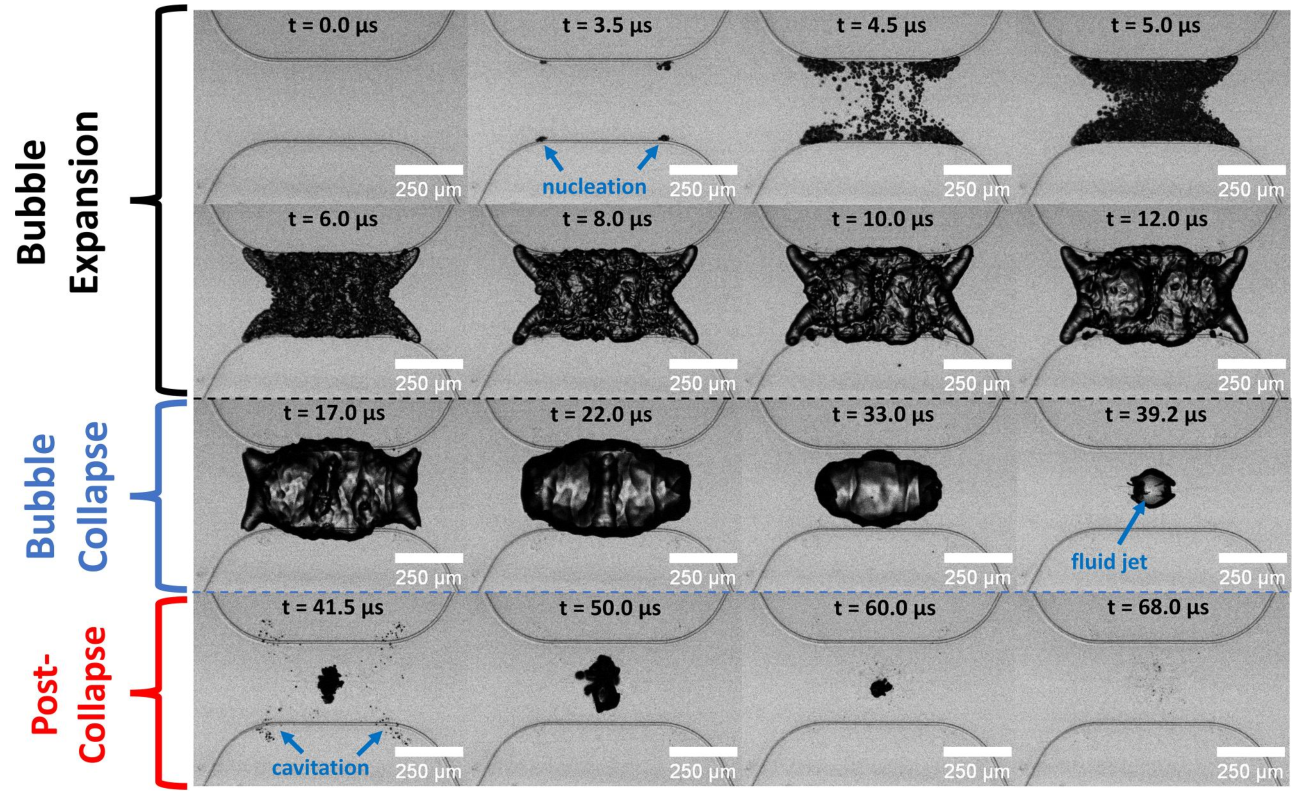

Figure 5. Vapor bubble dynamics illustrates the vapor bubble dynamics for a 300 x 700 μm^2, 8 Ω sq^{-1}, 44.99 Ω FTO resistor with 250 μm fillets on each corner and water covering its surface. We note these are unconfined resistors that are not in a channel. A firing pulse of $\tau = 5$ μs at $V = 100$ V was used to cause explosive boiling on the resistor's surface. The vapor bubble dynamics were imaged at 10 Mfps. Initially, the vapor bubble nucleates at the resistor's corners, $t = 3.5$ μs, where the heat flux is the greatest; after which, the vapor bubble grows and blankets the resistor's surface, $t = 5.0$ μs. The vapor bubble loses energy as it continues to expand reaching its maximum volume at $t = 12.0$ μs. Then, the vapor bubble rapidly collapses at high velocities which creates fluid jets impinging in the vapor upon collapse, $t = 39.2$ μs. During post-collapse, the vapor bubble collapse creates a region of low pressure which causes cavitation, $t = 41.5$ μs, and vapor bubble rebound until the vapor bubble fully dissolves back into the subcooled fluid, $t = 68.0$ μs.

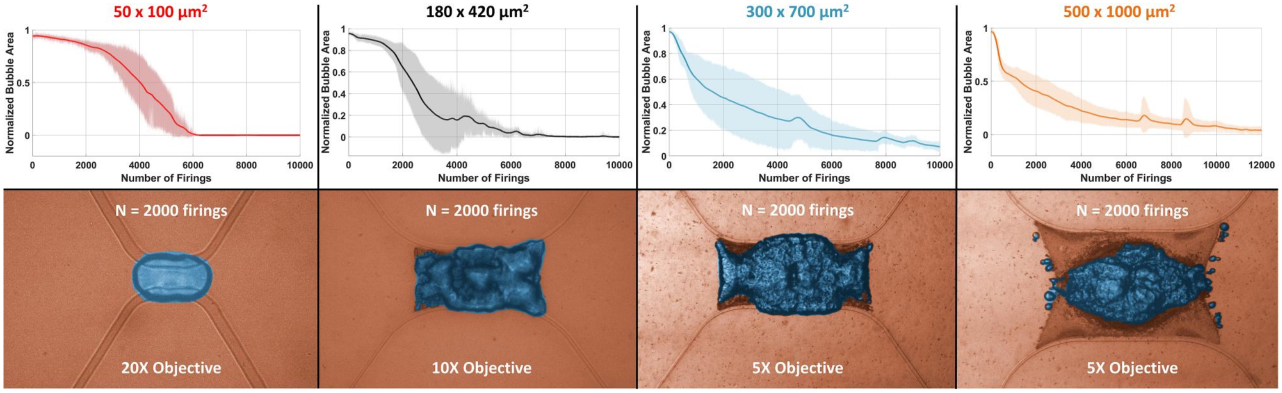

Figure 6. Albumin organic fouling resistor size variability illustrates sample variability of the normalized vapor bubble area as a function of the number of firing events for 50 x 100, 180 x 420, 300 x 700, and 500 x 1000 μm^2 resistor sizes. All resistors were tested using a 1 g dL^{-1} DI water solution of egg albumin and 5 sample replicates for each resistor size. The solid line represents the mean of the moving averages for each sample replicate while the shaded area represents one standard deviation from the mean. The segmented images display the trained RESNET-18 network identified vapor bubble areas at N = 2000 firing events.

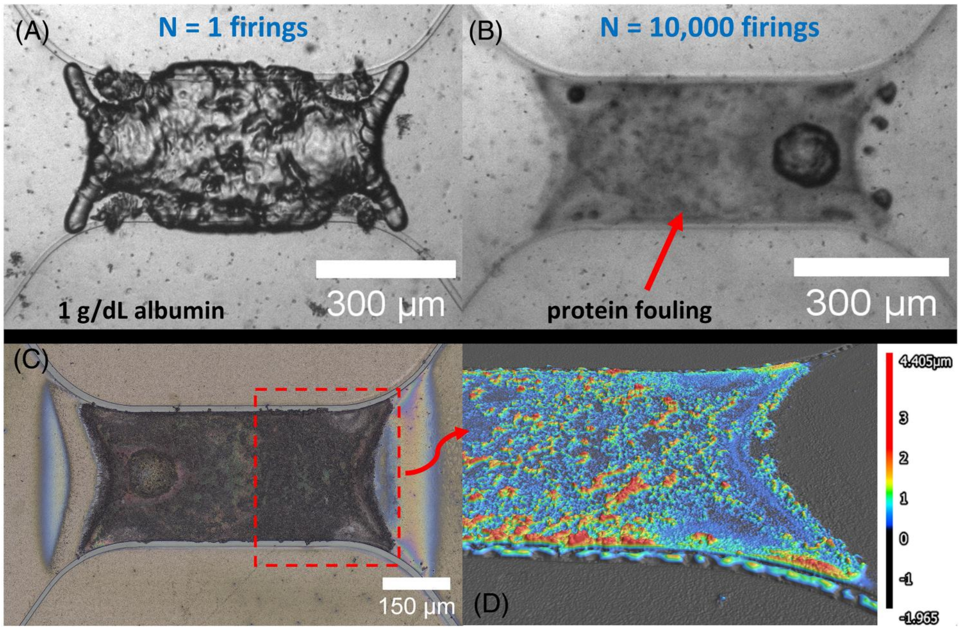

Figure 7. Fouling film micrograph illustrates Keyence VK-X1100 optical profilometry of the fouling film buildup on thermal bubble-driven micro-pumps. In (a-b), stroboscopic high-speed images of the vapor bubble at N = 1 firings and N = 10,000 firings in a 1 g dL^{-1} DI water solution of egg albumin are shown. In (c-d), the fouling layer is characterized after N = 10,000 firings. The average fouling layer thickness was 0.661 μm.

μm^2 resistors evident by the initial rapid decrease in vapor bubble area within $N = 2000$ firing events while, for the 180×420 μm^2 resistors, the fastest protein residue growth occurred during $N = 2000$ and $N = 4000$ firing events. For the 50×100 μm^2 resistors, the fastest protein residue growth occurred during $N = 3000$ and $N = 5000$ firing events. As seen in the segmented images of Figure 6, the trained RESNET-18 network successfully identifies the vapor bubble regions for each resistor size.

After 10,000 firing events, the normalized vapor bubble area approaches 0 which indicates that the protein residue growth fully encompasses the resistor active area. To characterize the protein residue, laser confocal surface profilometry was performed on a sample 300×700 μm^2 resistor at the end of 10,000 firing events using a Keyence VK-X1100 optical profilometer, shown in Figure 7. The growth of the protein residue over 10,000 firing events is evident on the resistor's surface in the stroboscopic images of the vapor bubble, Figure 7a and b. Zooming in on the protein residue, Figure 7c and d, it can be seen that there is a film between 0-4 μm coating the surface of the resistor, average film thickness was 0.661 μm. We

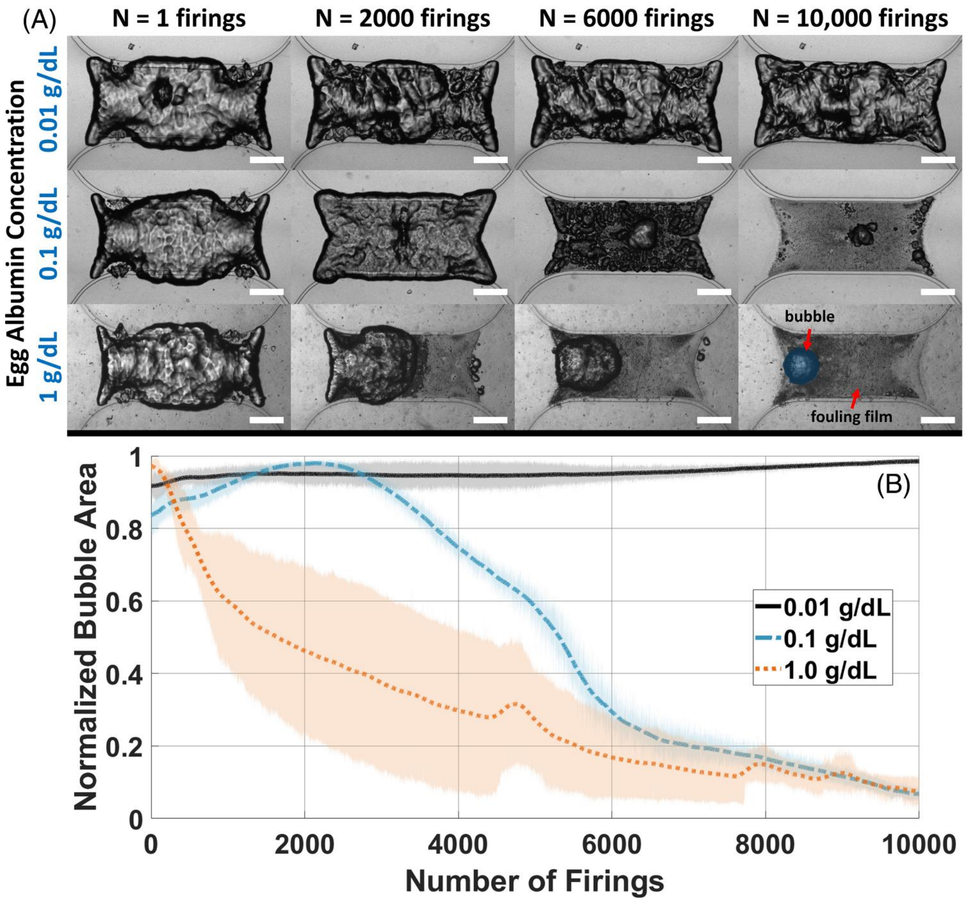

Figure 8. Concentration dependence of egg albumin fouling depicts the effect of concentration on organic fouling of 300 x 700 μm^2 thermal bubble-driven micro-pumps with egg albumin. Concentration of egg albumin in DI water was varied from 1 g dL^{-1} to 0.01 g dL^{-1}. For each concentration, 5 resistors were tested for N = 10,000 firing events. (a) shows stroboscopic images of the resistor's surface at N = 1, 2000, 6000, and 10,000 firing events for each concentration. (b) shows the normalized bubble area as a function of the number of firing events for each concentration. Shaded error regions represent one standard deviation from the mean. A moving average filter of k = 200 data points was used. Scale bar is 150 μm.

hypothesize that this protein residue inhibits the heat transfer between the thin film resistor and the working fluid, which is consistent with literature, and causes the vapor bubble area to decrease. Once the protein residue covers the resistor's active area, the vapor bubble area approaches 0 and thus the flow rate of the micro-pump would also approach 0.

Concentration dependence of egg albumin fouling

The extent and rate of fouling is dependent on biofluid concentration. Thus, dilution of a biofluid can be used to reduce surface fouling enabling compatibility with thermal bubble-driven micro-pumps. Figure 8 illustrates the effect of diluting egg albumin with DI water on the extent and rate of fouling. At low concentration (0.01 g dL^{-1}, 100X smaller than the concentration of albumin in human blood), there is no observable fouling. In fact, perhaps unintuitively, the vapor bubble area increases as a function of firing events. This trend is likely due to thermal buildup of heat from successive firing events which increases the vapor bubble size. When the solute loading is 10X higher (0.1 g dL^{-1}), a fouling layer forms over the surface of the resistor and the vapor bubble decreases in size. The initial rise in normalized bubble area from $N=0$ to $N=2000$ firing events is due to the shape of the vapor bubble flattening, Figure 8a. As the fouling layer grows, the vapor bubble area decreases until near 0. At 1.0 g dL^{-1}, the fouling layer quickly forms resulting in a steep decrease in the bubble area. Additionally, the variability at 1.0 g dL^{-1} is large suggesting that high concentrations of albumin result in a more stochastic fouling process than lower concentrations. Although diluting egg albumin in DI water successfully reduced the extent and rate of fouling on thermal bubble-driven micro-pumps, the amount of solute loading required for negligible

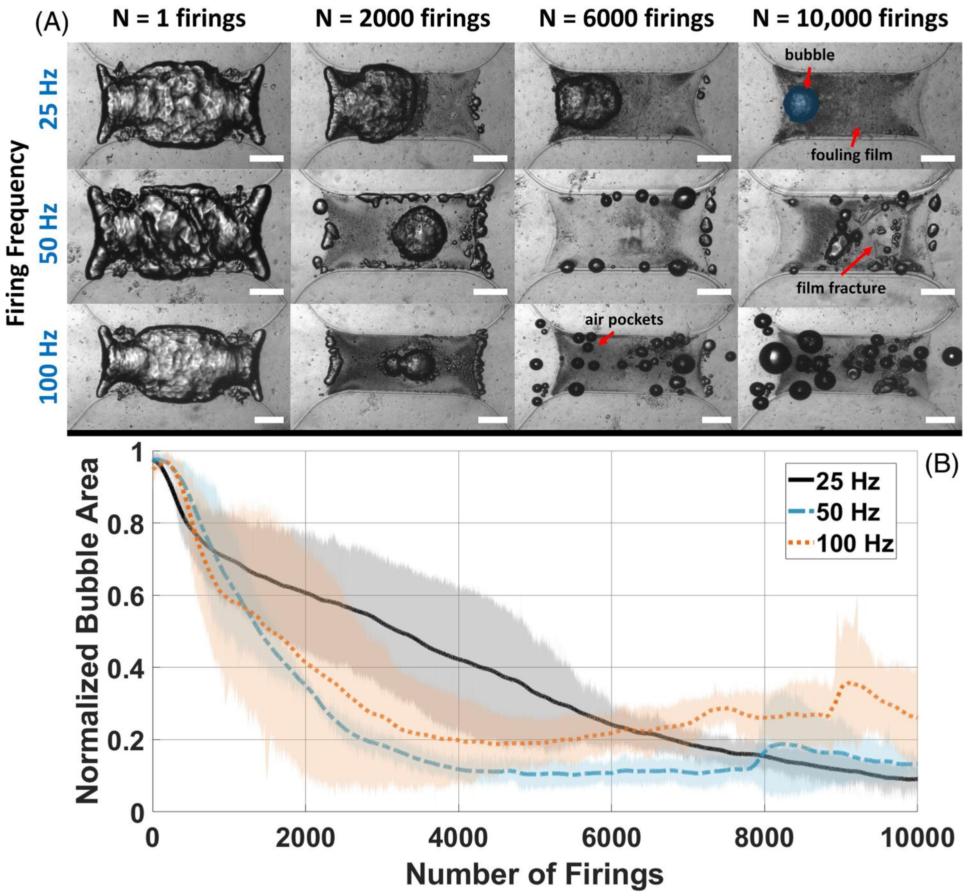

Figure 9. Firing frequency dependence of egg albumin fouling depicts the effect of firing frequency on organic fouling of 300 x 700 μm^2 thermal bubble-driven micro-pumps with egg albumin. Concentration of egg albumin in DI water was 1 g dL^{-1}. For each firing frequency, 3 resistors were tested for N = 10,000 firing events. (a) shows stroboscopic images of the resistor's surface at N = 1, 2000, 6000, and 10,000 firing events for each firing frequency. (b) shows the normalized bubble area as a function of the number of firing events for each firing frequency. Shaded error regions represent one standard deviation from the mean. A moving average filter of k = 200 data points was used. Scale bar is 150 μm.

fouling over $N = 10{,}000$ firing events ($0.01\,\mathrm{g\ dL^{-1}}$) is approximately 100X lower than the concentration of albumin in human blood. Low solute loading may cause reduced sensitivity and low throughput for applications requiring processing of biofluids. Therefore, although a biofluid can be made compatible with thermal bubble-driven micro-pumps through dilution, it may not be compatible with the microfluidic application of interest.

Firing frequency dependence of egg albumin fouling

In addition to biofluid concentration, the rate of fouling is dependent on the firing frequency. As the firing frequency increases, residual heat buildup in the substrate, see Figure S2, results in a higher nucleation temperature in the fluid which likely increases the rate of fouling. Figure 9 illustrates the effect of firing frequency on fouling with a $1\,\mathrm{g\ dL^{-1}}$ solution of egg albumin protein in DI water. The rate of fouling increases with increased firing frequency, Figure 9a. Additionally, in the 50 Hz case study, after $N = 10{,}000$ firing events, we observed that the fouling layer fractured and lifted off of the resistor's surface. However, we note that a surface fouling layer likely remains on the resistor's surface since despite the fouling layer fracturing, vapor bubble nucleation was still inhibited. Interestingly, at 100 Hz and $N = 6000$ firing events, we observed air pockets forming near the resistor's surface. We postulate that these air pockets are dissolved gases present in the fluid (not degassed a priori) which are more prominent at higher firing frequencies likely due to an increased fluid working temperature since less time between firing events means the working fluid will be hotter at higher firing frequencies. Quantifying the rate of fouling, initially, the rate of fouling across all firing frequencies is similar until approximately $N = 500$ firing events upon which fouling occurs faster for the 50 and 100 Hz cases than the 25 Hz case, shown in Figure 9b. Specifically,

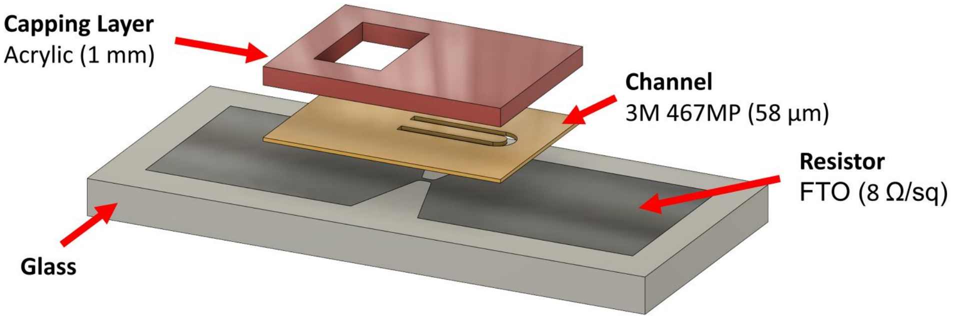

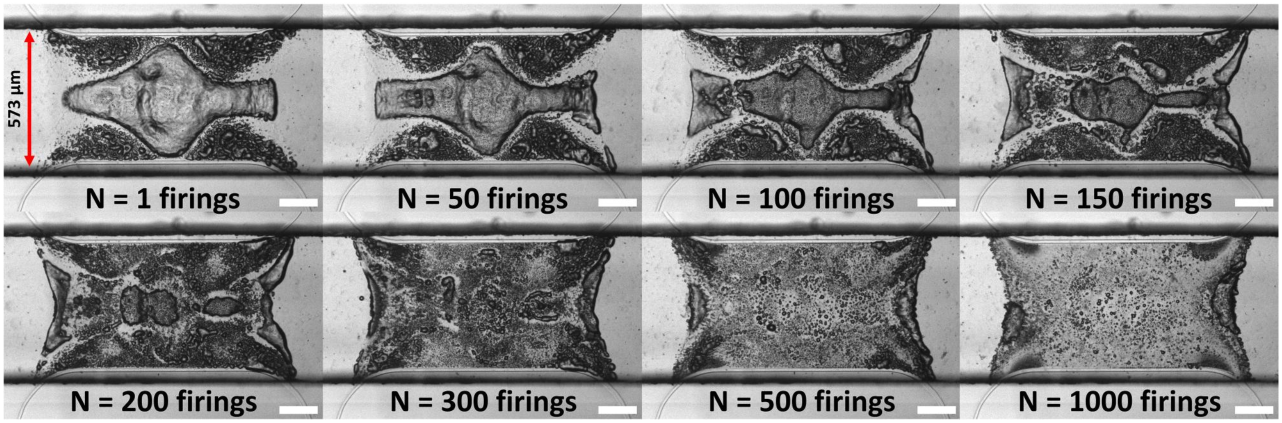

Figure 10. Egg albumin fouling during pumping depicts fouling dynamics during pumping of a 500 x 1000 μm^2 thermal bubble-driven micro-pump with 1 g dL^{-1} egg albumin in DI water at a firing frequency of 25 Hz. Stroboscopic images at $\tau = 10$ μs are shown across N = 1000 firing events. The flow rate was 5.97 nL $pulse^{-1}$, computed from flow of water in the channel. The channel length, width, and height were 11.588 mm, 573 μm, 332 μm respectively with the resistor placed 1752 μm from the reservoir. Scale bar is 150 μm.

complete fouling occurred near $N = 10{,}000$ firing events for the 25 Hz case in contrast to $N = 4000$ for the 50 and 100 Hz cases. Therefore, increased firing frequency results in a faster rate of fouling.

Egg albumin fouling during pumping

Previously, resistors were unconfined; that is, biofluid was placed directly over the resistor's surface. In a realistic microfluidic device with thermal bubble-driven micro-pumps, resistors are confined to a channel filled with biofluid and each firing pulse results in fluid flow over the resistor's surface. To investigate fouling dynamics under these more realistic flow conditions, a $500 \times 1000\ \mu m^2$ resistor was placed in a U-shaped channel filled with 1 g dL^{-1} solution of DI water and egg albumin, shown in Figure 10. The channel length, width, and height were 11.588 mm, 573 μm, 332 μm respectively with the resistor placed 1752 μm from the reservoir. Before egg albumin solution was added to the channels, the flow rate was measured in water, to ensure no fouling, using particle tracking velocimetry of 27–32 μm diameter neutrally buoyant micro-spheres (Cospheric Inc., Goleta, CA, USA), detailed methods can be found in our past work (Hayes et al. 2022). The flow rate was measured to be 5.97 nL $pulse^{-1}$. After the channel was purged with DI water and dried, a 1 g dL^{-1} solution of DI water and egg albumin was added to study fouling dynamics during pumping. Figure 10 illustrates the fouling process during pumping over $N = 2000$ firing events, also see movie S1. Despite fluid flow over the resistor's surface, a fouling layer builds and prevents vapor bubble nucleation after approximately $N = 500$ firing events. We note that the rate of complete fouling is significantly faster when confined ($N = 500$ firings) versus unconfined ($N = 8000$ firings), see Figure 6. We hypothesize that this is due to the working fluid reaching a greater temperature in the confined case versus the unconfined case due to differences in the volume of fluid exposed to the resistor. In the confined case, the volume of fluid exposed to the resistor is approximately the area of the resistor multiplied by the channel height or $V = 573\ \mu m \text{ x } 332\ \mu m \text{ x } 1000\ \mu m = 0.19\ \mu L$ whereas, in the unconfined case, a $V \approx 2$ mL droplet of fluid is added over the resistor's surface. Thus, we postulate that the vortexes and bulk fluid flow caused by the vapor bubble recirculate fluid to a greater extent when unconfined versus confined

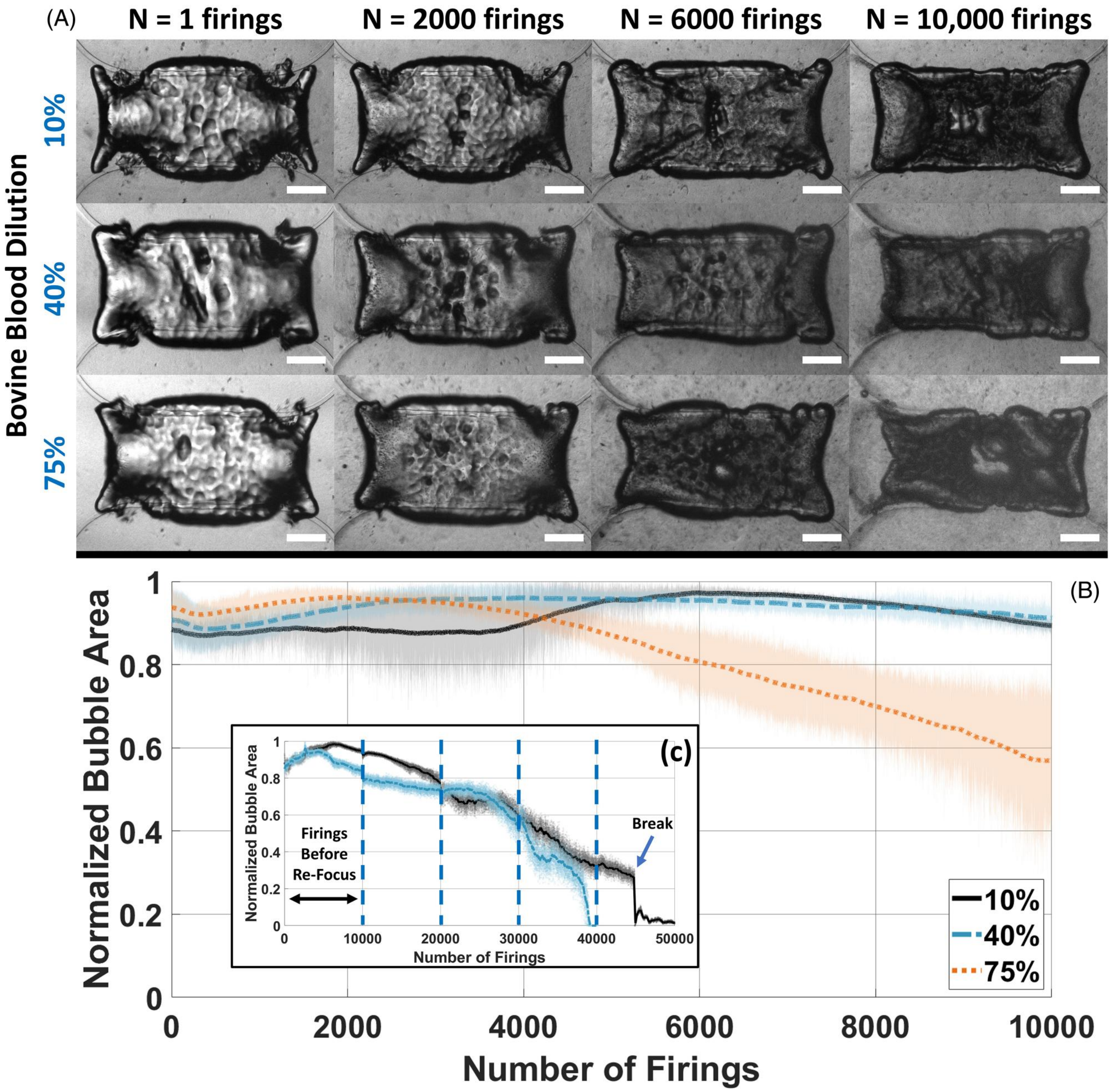

Figure 11. Concentration dependence of defibrinated bovine blood fouling depicts the effect of concentration on organic fouling of 300 x 700 μm^2 thermal bubble-driven micro-pumps using defibrinated bovine blood. Bovine blood was diluted in DI water from 10% to 75% weight percent. For each concentration, 5 resistors were tested for $N = 10,000$ firing events. (a) shows stroboscopic images of the resistor's surface at $N = 1$, 2000, 6000, and 10,000 firing events for each concentration. (b) shows the normalized bubble area as a function of the number of firing events for each concentration. Shaded error regions represent one standard deviation from the mean. A moving average filter of $k = 200$ data points was used. (c) shows extended firing tests for two resistors in 10% and 40% weight percent bovine blood. After every 10,000 firings, the microscope was re-focused on the vapor bubble to maintain image quality due to a lensing effect from evaporation of the biofluid. We note that the 75% case was terminated after 10,000 firing events because suspended particulate matter prevented imaging. Scale bar is 150 µm.

resulting in a greater rate of fouling when a resistor is confined to a micro-channel.

Fouling with defibrinated bovine blood

Biofluids, such as blood, are a complex mixture of proteins, cells, and fluids, all of which could induce fouling on a thermal bubble-driven micro-pump. In Sections "Fouling with egg albumin" and "Concentration dependence of egg albumin fouling", egg albumin was used to simplify the interaction between biofluid and micro-pump since only one protein was present in the mixture; thus, only one protein caused fouling on the resistor's surface. However, a realistic biofluid is more complex and could consist of many different proteins and cell types. Here, we utilize defibrinated bovine blood to create mixtures with DI water of different weight percent bovine blood. Whole defibrinated bovine blood (100% weight percent) could not be used in this study as the transmission of light was too low to image vapor bubble dynamics. As such, dilutions of 10%, 40%, and 75% weight percent bovine blood in DI water were used. Figure 11 illustrates the interaction between defibrinated bovine blood and thermal bubble-driven micro-pumps of size $300 \times 700\ \mu m^2$ for each concentration. At a dilution of 10% and 40% bovine blood, the vapor bubble flattens and the normalized vapor bubble area decreases to 90% the initial bubble area within $N = 10{,}000$ firing events. Beyond 10,000 firing events, Figure 11c shows that the fouling layer grows and the normalized bubble area decreases until the resistor breaks. Beyond approximately 10 min of firings (or 10,000 firing events), we note that the microscope must be re-focused on the resistor to maintain high image quality as evaporation of the fluid causes the focal plane to shift. Thus, we re-focused the microscope after every 10,000 firing events as denoted by the dashed lines in Figure 11c. At a dilution of 75% bovine blood, fouling occurs more rapidly in which the normalized vapor bubble area decreases to 50% the initial bubble area within $N = 10{,}000$ firing events. To our knowledge, this is the first work that has demonstrated that a thermal generated vapor bubble can be formed in blood; however, we note that fouling layer buildup on the resistor's surface decreases the vapor bubble area as a function of firing events and thus the pump performance also decreases as the number of firing events increase. In this work, we have found micro-pump lifetimes to be 2000-10,000 firing events, which corresponds to an approximate pumping capability of 6.4-32 μL for a $300 \times 700\ \mu m^2$ resistor (Hayes et al. 2022). While this pumping capability may be sufficient for a disposable microfluidic biomedical system, we anticipate the need for a greater micro-pump lifetime. As such, we envision mitigation strategies to prevent fouling as a key step to enable widespread use of this technology for biomedical applications which will be the focus of future work.

Conclusions

Despite the promise of thermal bubble-driven micro-pumps enabling lab-on-a-chip technologies, little work has been done on the compatibility and use of these micro-pumps with biofluids. Before expanding into healthcare applications, fundamental work must first be performed demonstrating (a) an approach to characterize fouling on these micro-pumps, (b) compatibility of these micro-pumps with protein-rich and cell-laden fluids, and (c) mitigation strategies to prevent fouling. This study addresses the first two points. In this work, we describe a characterization methodology using deep learning image segmentation to quantify the amount of fouling on a thermal bubble-driven micro-pump as a function of the number of firing events. Additionally, we demonstrate that thermal generated vapor bubbles are compatible with both protein-rich (egg albumin mixtures) and cell-laden (defibrinated bovine blood) biofluids. However, it was shown that high concentrations of egg albumin and defibrinated bovine blood cause a large degree of surface fouling on thermal bubble-driven micro-pumps which reduce lifetime and pump performance. Thus, a mitigation strategy is needed to prevent fouling on thermal bubble-driven micro-pumps with biofluids which is the focus of future work. In applications of thermal bubble-driven micro-pumps for healthcare, it will be required to process and manipulate protein-rich and cell-laden fluids. As such, this work provides a foundation to understand and characterize fouling of thermal bubble-driven micro-pumps.

Acknowledgements

Any opinion, findings, and conclusions or recommendations expressed in this material are those of the author(s) and do not necessarily reflect the views of the National Science Foundation.

Disclosure statement

No potential conflict of interest was reported by the author(s).

Funding

This work is supported by startup funds to R. MacCurdy provided by the University of Colorado Boulder as well as the National Science Foundation Graduate Research Fellowship under Grant No. DGE 1650115.

References

Alhuthali S, Delaplace G, Macchietto S, Bouvier L. 2022. Whey protein fouling prediction in plate heat exchanger by combining dynamic modelling, dimensional analysis, and symbolic regression. Food Bioprod Process. 134:163–180. https://www.sciencedirect.com/science/article/pii/S0960308522000608. doi: 10.1016/j.fbp.2022.05.009.

Bar-Levav E, Witman M, Einat M. 2020. Thin-film mems resistors with enhanced lifetime for thermal inkjet. Micromachines (Basel). 11:499. https://www.mdpi.com/2072-666X/11/5/499. doi: 10.3390/mi11050499.

Bhattacharjee N, Urrios A, Kang S, Folch A. 2016. The upcoming 3d-printing revolution in microfluidics. Lab Chip. 16:1720–1742. doi: 10.1039/C6LC00163G.

Bogahawaththa D, Vasiljevic T. 2022. Shear-induced structural changes and denaturation of bovine immunoglobulin g and serum albumin at different temperatures. Food Hydrocolloids. 124:107283. https://www.sciencedirect.com/science/article/pii/S0268005X21006998. doi: https://doi.org/10.1016/j.foodhyd.2021.107283.

Chin CD, Laksanasopin T, Cheung YK, Steinmiller D, Linder V, Parsa H, Wang J, Moore H, Umviligihozo RRG, Karita E, et al. 2011. Microfluidics-based diagnostics of infectious diseases in the developing world. Nat Med. 17:1015–1019. doi: 10.1038/nm.2408.

de Almeida CF, Saget M, Delaplace G, Jimenez M, Fierro V, Celzard A. 2023. Innovative fouling-resistant materials for industrial heat exchangers: a review. Rev Chem Engin. 39:71–104 [cited 2023-07-17]. doi: 10.1515/revce-2020-0094.

Einat M, Grajower M. 2010. Microboiling measurements of thermal-inkjet heaters. J Microelectromech Syst. 19:391–395. doi: 10.1109/JMEMS.2010.2040946.

Elofsson UM, Paulsson MA, Sellers P, Arnebrant T. 1996. Adsorption during heat treatment related to the thermal unfolding/aggregation of -lactoglobulins A and B. J Colloid Interface Sci. 183:408–415. doi: 10.1006/jcis.1996.0563. https://www.sciencedirect.com/science/article/pii/S0021979796905639.

Gómez-Sjöberg R, Leyrat AA, Pirone DM, Chen CS, Quake SR. 2007. Versatile, fully automated, microfluidic cell culture system. Anal Chem. 79:8557–8563. pMID: 17953452. arXiv: doi:10.1021/ac071311w.

Govyadinov A, Kornilovitch P, Markel D, Torniainen E. 2016. Single pulse dynamics and flow rates of inertial micropumps. Microfluid Nanofluid. 20:73. doi: 10.1007/s10404-016-1738-x.

Hashemzadeh H, Shojaeilangari S, Allahverdi A, Rothbauer M, Ertl P, Naderi-Manesh H. 2021. A combined microfluidic deep learning approach for lung cancer cell high throughput screening toward automatic cancer screening applications. Sci Rep. 11:9804. doi: 10.1038/s41598-021-89352-8.

Hayes B, Govyadinov A, Kornilovitch P. 2018. Microfluidic switchboards with integrated inertial pumps. Microfluid Nanofluid. 22:15. doi: 10.1007/s10404-017-2032-2.

Hayes B, Smith L, Kabutz H, Hayes AC, Whiting GL, Jayaram K, MacCurdy R. 2022. Rapid fabrication of low-cost thermal bubble-driven micropumps. Micromachines 13 (10). https://www.mdpi.com/2072-666X/13/10/1634. doi: 10.3390/mi13101634.

Hedayati M, Marruecos DF, Krapf D, Kaar JL, Kipper MJ. 2020. Protein adsorption measurements on low fouling and ultralow fouling surfaces: a critical comparison of surface characterization techniques. Acta Biomater. 102:169–180. doi: 10.1016/j.actbio.2019.11.019. https://www.sciencedirect.com/science/article/pii/S1742706119307603.

Henry C, Minier J-P, Lefèvre G. 2012. Towards a description of particulate fouling: from single particle deposition to clogging. Adv Colloid Interface Sci. 185–186:34–76. doi: https://doi.org/10.1016/j.cis.2012.10.001.https://www.sciencedirect.com/science/article/pii/S0001868612001418.

Hung PJ, Lee PJ, Sabounchi P, Lin R, Lee LP. 2005. Continuous perfusion microfluidic cell culture array for high-throughput cell-based assays. Biotechnol Bioeng. 89:1–8. https://onlinelibrary.wiley.com/doi/pdf/10.1002/bit.20289. https://onlinelibrary.wiley.com/doi/abs/10.1002/bit.20289. doi: 10.1002/bit.20289.

Jeurnink T, Verheul M, Stuart MC, de Kruif C. 1996. Deposition of heated whey proteins on a chromium oxide surface. Colloids Surf, B. 6:291–307. https://www.sciencedirect.com/science/article/pii/0927776595012621. doi: 10.1016/0927-7765(95)01262-1.

Kornilovitch P, Govyadinov A, Markel D, Torniainen E. 2013. Onedimensional model of inertial pumping. Phys Rev E. 87:023012. doi: 10.1103/PhysRevE.87.023012.

Kornilovitch PE, Cochell T, Govyadinov AN. 2022. Temperature dependence of inertial pumping in microchannels. Phys Fluids. 34:022003. doi: 10.1063/5.0079327.

Lepock JR. 1997. Protein denaturation during heat shock. Adv Mol Cell Biol. 19:223–259. doi: 10.1016/S1569-2558(08)60079-X. https://www.sciencedirect.com/science/article/pii/S156925580860079X.

Liu D, Zhang H, Fontana F, Hirvonen JT, Santos HA. 2017. Microfluidicassisted fabrication of carriers for controlled drug delivery. Lab Chip. 17:1856–1883. doi: 10.1039/C7LC00242D.

Liu Y, Yang G, Hui Y, Ranaweera S, Zhao C-X. 2022. Microfluidic nanoparticles for drug delivery. Small. 18:2106580. https://onlinelibrary.wiley.com/doi/pdf/10.1002/smll.202106580. https://onlinelibrary.wiley.com/doi/abs/10.1002/smll.202106580. doi: 10.1002/smll.202106580.

Lu J, Su T, Thirtle P, Thomas R, Rennie A, Cubitt R. 1998. The denaturation of lysozyme layers adsorbed at the hydrophobic solid/liquid surface studied by neutron reflection. J Colloid Interface Sci. 206:212–223. https://www.sciencedirect.com/science/article/pii/S0021979798956806. doi: 10.1006/jcis.1998.5680.

Mahdi Y, Mouheb A, Oufer L. 2009. A dynamic model for milk fouling in a plate heat exchanger. Appl Math Modell. 33:648–662. https://www.sciencedirect.com/science/article/pii/S0307904X07003162. doi: 10.1016/j.apm.2007.11.030.

Marcus JS, Anderson WF, Quake SR. 2006. Parallel picoliter RT-PCR assays using microfluidics. Anal Chem. 78:956–958., doi:10.1021/ac0513865. URL doi: 10.1021/ac0513865.

Mohammed MI, Haswell S, Gibson I. 2015. Lab-on-a-chip or chip-in-a-lab: Challenges of commercialization lost in translation, Procedia Technology 20 (2015) 54–59, Proceedings of the 1st International Design Technology Conference, DESTECH 2015, Geelong. doi: 10.1016/j.protcy.2015.07.010. https://www.sciencedirect.com/science/article/pii/S2212017315001875.

Nivedita N, Papautsky I. 2013. Continuous separation of blood cells in spiral microfluidic devices. Biomicrofluidics. 7:54101. https://pubs.aip.org/aip/bmf/article-pdf/doi/10.1063/1.4819275/9268038/054101/_1/_online.pdf. doi: 10.1063/1.4819275.

Ory E, Yuan H, Prosperetti A, Popinet S, Zaleski S. 2000. Growth and collapse of a vapor bubble in a narrow tube. Phys Fluids. 12:1268–1277. doi: 10.1063/1.870381.

Preetam S, Nahak BK, Patra S, Toncu DC, Park S, Syväjärvi M, Orive G, Tiwari A. 2022. Emergence of microfluidics for next generation biomedical devices. Biosensors and Bioelectronics: X. 10:100106. doi: 10.1016/j.biosx.2022.100106. https://www.sciencedirect.com/science/article/pii/S2590137022000024.

Ruiz O. 2007. CFD Model of the thermal inkjet droplet ejection process. Vol. 3, Heat Transfer Summer Conference. p. 357–365. doi: 10.1115/HT2007-32427.

Salim B, Athira MV, Kandaswamy A, Vijayakumar M, Saravanan T, Sairam T. 2017. Microfluidic device for novel breast cancer screening by blood test using mirna beacon probe. Biomed Microdevices. 19:89. doi: 10.1007/s10544-017-0230-z.

Schultz MP. 2007. Effects of coating roughness and biofouling on ship resistance and powering. Biofouling. 23:331–341. ., . doi: 10.1080/08927010701461974.

Steel BC, McKenzie DR, Bilek MM, Nosworthy NJ, dos Remedios CG. 2006. Nanosecond responses of proteins to ultra-high temperature pulses. Biophys J. 91:L66–L68. https://www.sciencedirect.com/science/article/pii/S0006349506719142. doi: 10.1529/biophysj.106.090944.

Supekar OD, Brown JJ, Greenberg AR, Gopinath JT, Bright VM. 2018. Real-time detection of reverse-osmosis membrane scaling via raman spectroscopy. Ind Eng Chem Res. 57:16021–16026.,. doi:10.1021/acs.iecr.8b01272. doi: 10.1021/acs.iecr.8b01272.

Torniainen ED, Govyadinov AN, Markel DP, Kornilovitch PE. 2012. Bubble-driven inertial micropump. Phys Fluids. 24:122003. https://pubs.aip.org/aip/pof/article-pdf/doi/10.1063/1.4769755/13433326/122003/_1/_online.pdf. doi: 10.1063/1.4769755.

Yang S, Undar A, Zahn JD. 2006. A microfluidic device for continuous, real time blood plasma separation. Lab Chip. 6:871–880. doi: 10.1039/B516401J.

Yin Z, Prosperetti A. 2005. ‘blinking bubble’ micropump with microfabricated heaters. J Micromech Microeng. 15:1683–1691. doi: 10.1088/0960-1317/15/9/010.

Yuan H, Prosperetti A. 1999. The pumping effect of growing and collapsing bubbles in a tube. J Micromech Microeng. 9:402–413. doi: 10.1088/0960-1317/9/4/318.

Zhang C, Xu J, Ma W, Zheng W. 2006. PCR microfluidic devices for DNA amplification. Biotechnol Adv. 24:243–284. https://www.sciencedirect.com/science/article/pii/S0734975005001254. doi: 10.1016/j.biotechadv.2005.10.002.